



Determining the nature of quantum resonances by probing elastic and reactive scattering in cold collisions

Prerna Paliwal^{1,4}, Nabanita Deb^{1,4}, Daniel M. Reich², Ad van der Avoird³, Christiane P. Koch²✉ and Edvardas Narevicius¹✉

Scattering resonances play a central role in collision processes in physics and chemistry. They help build an intuitive understanding of the collision dynamics due to the spatial localization of the scattering wavefunctions. For resonances that are localized in the reaction region, located at short separation behind the centrifugal barrier, sharp peaks in the reaction rates are the characteristic signature, observed recently with state-of-the-art experiments in low-energy collisions. If, however, the localization occurs outside of the reaction region, mostly the elastic scattering is modified. This may occur due to above-barrier resonances, the quantum analogue of classical orbiting. By probing both elastic and inelastic scattering of metastable helium with deuterium molecules in merged-beam experiments, we differentiate between the nature of quantum resonances—tunnelling resonances versus above-barrier resonances—and corroborate our findings by calculating the corresponding scattering wavefunctions.

A scattering resonance, or temporary low-energy collision complex, can be formed by various mechanisms^{1,2}. Trapping of the colliding particles can occur due to the transfer of relative kinetic energy to other degrees of freedom, giving rise to Feshbach resonances^{3,4}. These are nowadays routinely used to tune interactions, for example, between cold atoms⁵ or atoms and molecules⁶. Feshbach resonances arise from the coupling of scattering states to a bound state that belongs to another scattering channel that is asymptotically characterized by a different set of quantum numbers. The coupling to a bound state results in a resonance wavefunction that is localized at a short interaction range.

On the other hand, shape and orbiting resonances form on a single potential curve that possesses a barrier. Although shape resonances are typically associated with tunnelling through the barrier, a resonance may also arise due to quantum reflection above the barrier. We refer to the resonances formed on or above the barrier as orbiting resonances, due to their analogy with classical orbiting. This distinction is important as the wavefunction of an orbiting resonance—in contrast to those of Feshbach and shape resonances—is highly delocalized and the collision complex is thus short-lived.

In reactions and inelastic processes, which can be described by capture models that separate long- and short-range dynamics^{7,8}, a resonance state localized at short separation behind the centrifugal barrier will have the strongest effect. By contrast, a resonance that hovers above the centrifugal barrier will be more relevant for elastic scattering. As such, investigation of both elastic and short-range-dominated inelastic channels is a convenient way to probe the localization of the resonance wavefunction and unequivocally identify the different underlying physical mechanisms.

To observe quantum resonances in the scattering experiments, one needs to reach collision energies (E/k_B) that correspond to a few kelvin. Such scattering resonances were first identified in

pioneering experiments performed by Scoles and co-workers⁹, with resonances clearly resolved by Toennies and colleagues^{10–13}, where a crossed-beam set-up was used to achieve collision energies that

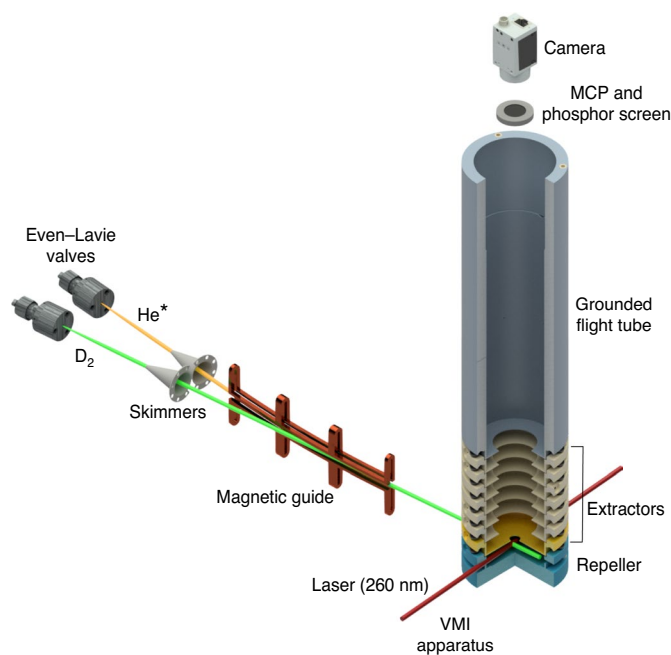


Fig. 1 | Experimental set-up. Supersonic beams of D₂ and He* are produced by two pulsed Even-Lavie valves and merged using a magnetic guide. A 260 nm laser is then used to single-photon ionize He* atoms that are subsequently detected via VMI set-up.

¹Department of Chemical and Biological Physics, Weizmann Institute of Science, Rehovot, Israel. ²Dahlem Center for Complex Quantum Systems and Fachbereich Physik, Freie Universität Berlin, Berlin, Germany. ³Institute of Theoretical Chemistry, Institute for Molecules and Materials, Radboud University, Nijmegen, Netherlands. ⁴These authors contributed equally: Prerna Paliwal, Nabanita Deb. ✉e-mail: christiane.koch@fu-berlin.de; edvardas.narevicius@weizmann.ac.il

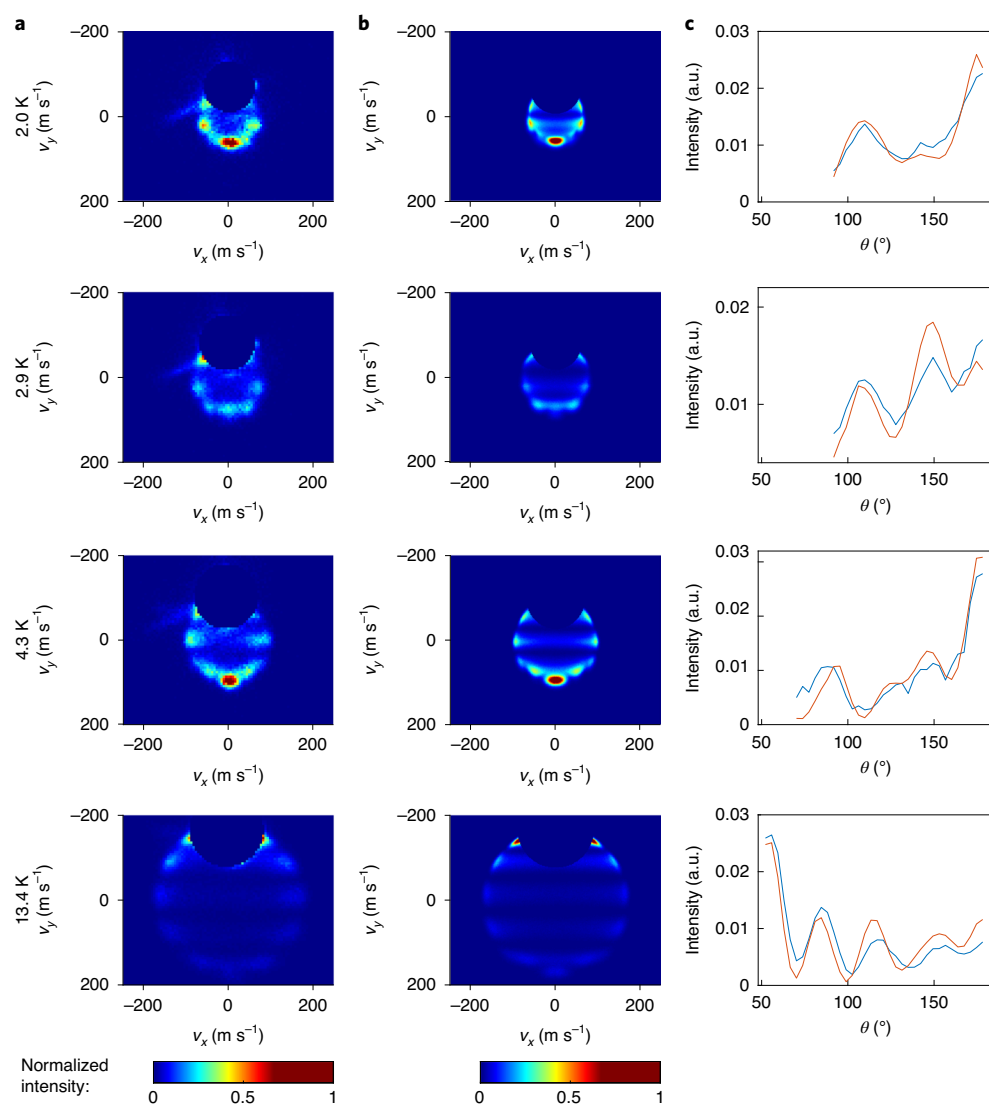


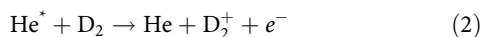
Fig. 2 | VMI images and angular distributions. **a, b**, The experimental and simulated VMI images are shown in **a** and **b**, respectively. The x- and y-axes refer to the velocity of He^+ in the centre-of-mass frame. The y-axis is the direction of the relative velocity vector, with the forward direction ($\theta=0^\circ$) pointing up in all of the images. The images are normalized to bring all the images to the same colour scale (see discussion in Methods). **c**, The angular distributions obtained from the images in **a** and **b** are shown as a function of scattering angle, θ , for experiments (blue curves) and simulations (red curves). a.u., arbitrary units.

correspond to 60 K and 5 K, respectively. Boesten and colleagues observed a shape resonance in cold atom scattering by pulsed photoassociation¹⁴. Dynamical Feshbach resonances were reported in the benchmark reaction ($\text{F}+\text{H}_2$ isotopologues) in crossed-beam experiments by Skodje et al.¹⁵ and Qiu et al.¹⁶ at collision energies down to 100 K. In a different approach, quantum resonances have also been identified by anion photoelectron spectroscopy by directly probing the transition state dynamics^{17,18}. With the recent success in reaching subkelvin collision energies using merged beams^{19,20}, shape resonances have also been detected in Penning ionization at a few millikelvin. Chefdeville et al. used a crossed-beam set-up to observe scattering resonances in inelastic molecular scattering at collision energies down to 5 K (ref. 21). Vogels et al. imaged inelastic scattering resonances using the velocity map imaging (VMI) technique together with a direct current electric field decelerator^{22,23}. Bergeat et al. studied inelastic scattering, observing resonances in the spin-orbit excitation of atomic carbon²⁴. Low-lying shape resonances have also been observed using pulsed-field-ionization

zero-kinetic-energy photoelectron spectroscopy in half-collisions of H^+-H and D^+-D (ref. 25).

Resonances in all previous experiments have been identified by observing peaks in the integrated cross-section, partial integrated cross-section²³ or backward-scattering spectrum²⁶ measured as a function of collision energy. So far, the nature of the resonances could only be inferred using theoretical analysis. Orbiting- and shape-type resonances may occur in both elastic and inelastic collisions, however, a different formation mechanism leads to sensitivity towards the range of interaction. To differentiate shape from orbiting resonances experimentally, one needs to be able to probe the localization of the resonance wavefunctions. Here we investigate two different processes for the same collision system that are sensitive to either the long- or short-range of the interaction potential to allow for this differentiation. In our experiments we identify scattering resonances in the elastic scattering (equation (1)) that probes the entire interaction range and compare it with the previously studied Penning ionization²⁷ (equation (2)) rate of helium

atoms in the 2^3S_1 metastable state (He^*) with D_2 , which is mainly sensitive to the short-range interaction.



Detecting and imaging low-energy resonances in the elastic scattering channel at a few kelvin is particularly challenging due to the small scattering angle of the products in the laboratory frame of reference. Here we use zero-energy electron recoil-assisted VMI together with the merged-beam technique to investigate low-energy elastic collisions. We are able to image above-barrier quantum resonances and elucidate their effect on observable quantities, thus distinguishing them from tunnelling resonances. We show that the reactive scattering is far more sensitive to tunnelling resonances that are localized at short internuclear distances, whereas both tunnelling and quantum reflection lead to formation of additional resonance structures detected in the elastic scattering process.

Results and discussion

The key to our ability to resolve resonances in the elastic differential cross-section (DCS) is the combination of the merged-beam technique¹⁹ with VMI²⁸ detection assisted by near-threshold photoionization and a low velocity spread of the reactants. The apparatus used in this study is illustrated in Fig. 1 and described in the Methods. We investigate the low-energy elastic scattering between He^* and normal D_2 (that is, two-thirds *ortho*- D_2 with $j=0$ and one-third *para*- D_2 with $j=1$, where j is the rotational quantum number). In our experiment, we probe elastically scattered He^* atoms by single-photon near-threshold ionization at 260 nm. This ensures that the electrons carry near-zero kinetic energy and thus avoid image blurring due to the photoelectron recoil effect²⁹. A narrow velocity spread of the He^* beam is another necessary condition for the measurement of the elastic scattering DCS. Our supersonic source—the Even–Lavie valve³⁰ combined with a dielectric barrier discharge—generates a 150 mK cold beam of He^* that localizes the unscattered part of atoms to a small area on our detector. Note that no internal state-changing collisions are possible in the collision energy range of our experiment; excitations are energetically not allowed and quenching is also not possible as the D_2 molecules that are produced by supersonic expansion are already in their lowest rovibrational state.

In Fig. 2 we present the VMI images of the scattered He^* obtained experimentally and simulated theoretically at different relative velocities corresponding to collision energies of 2.0 ± 0.1 K, 2.9 ± 0.2 K, 4.3 ± 0.2 K and 13.4 ± 0.5 K, with the error bars indicating the standard deviation. We have removed the forward part of the measured image, which is dominated by the direct He^* beam that does not undergo scattering. For clarity and comparison, we have also removed the corresponding area from the simulated images. As no inelastic scattering is possible at our experimental collision energies and the total energy is conserved for elastic collisions, the images show a single scattering ring with a radius proportional to the relative velocity. We also observe diffraction oscillations in all of the VMI images due to interference between different partial waves given by integer quantum number l . The maximum number of interfering partial waves is determined by collision energy. The bands obtained in the VMI images are a result of projecting the 3D sphere in momentum space onto a 2D microchannel plate (MCP) detector. The angular distributions reflect the DCSs of the collision process. The agreement between the calculated and measured angular distributions visible in Fig. 2 attests to the accuracy of the potential energy surface³¹.

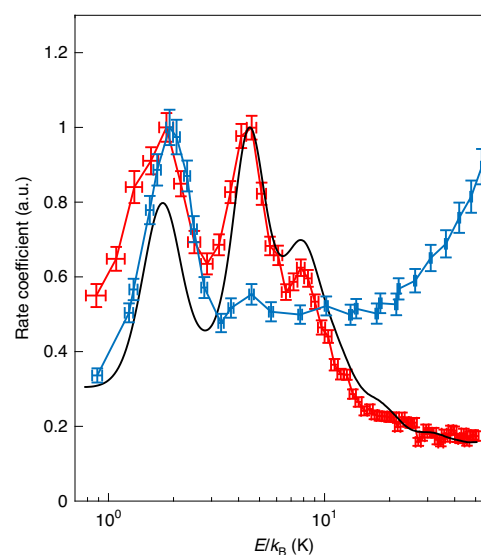


Fig. 3 | Relative rate coefficients versus collision energies for elastic scattering and Penning ionization of He^*-D_2 . The red data points with error bars denote the experimentally measured partial relative rate coefficient for the elastic scattering of He^*-D_2 where the scattering signal is integrated over the backward hemisphere. The black curve is the theoretically predicted partial relative rate coefficient for elastic scattering including full kinematics of the experiment (see Methods). The blue data points with error bars represent the experimentally measured relative rate coefficient for Penning ionization of the same system (from ref.²⁷). The error bars represent standard deviation in collision energy and rate coefficients. The red and blue lines are just joining the experimental data points. The relative scaling of the red and blue curve is arbitrary and is made equal to one at the energy corresponding to the first maxima of both curves.

In addition to the diffraction oscillations, the backward scattering is seen to be strongly enhanced in Fig. 2 at collision energies of 2.0 K and 4.3 K. As the collision energy approaches the resonant energy, a single partial-wave (l_{res}) structure—dictated by the square of the Legendre polynomial, $|P_{l_{\text{res}}}(\cos \theta)|^2$ —starts to dominate the angular distribution. This leads to an enhancement of forward-backward scattering and has also been reported for other systems^{22,23,32–34}. We measure the partial relative rate coefficient for the elastic collision between He^*-D_2 as a function of the collision energy to find the energy positions of these resonant states, as illustrated by the red curve in Fig. 3 for the collision energy range of 0.9–50 K. For a given energy, the partial rate coefficient is obtained by counting the number of He^* atoms scattered in the backward hemisphere ($\theta \geq 90^\circ$) of the image and scaling it by the product of the number of He^* in the reactant beam and D_2 beam intensity (see Methods). The black curve in Fig. 3 is the theoretically predicted partial rate coefficient, which is calculated by taking into account full kinematics of the experiment. We obtain the theoretical partial cross-section by performing close-coupling quantum scattering calculations for collisions with *ortho*- ($j=0$) and *para*- D_2 ($j=1$) using the theoretical framework established by Klein et al.³¹ (see Methods). A comparison of theoretically obtained partial and total rate coefficients for elastic scattering of He^* with normal D_2 is shown in Extended Data Fig. 1. The experimentally obtained partial rate coefficient in Fig. 3 shows good agreement with the theoretically predicted partial rate coefficient for the same energy range.

The blue curve in Fig. 3 also shows the rate coefficient obtained in previously performed Penning ionization experiments²⁷. The experimental curve shows a possible feature, predicted by theory²⁷ at 4.6 K, with its amplitude contained within the statistical error;

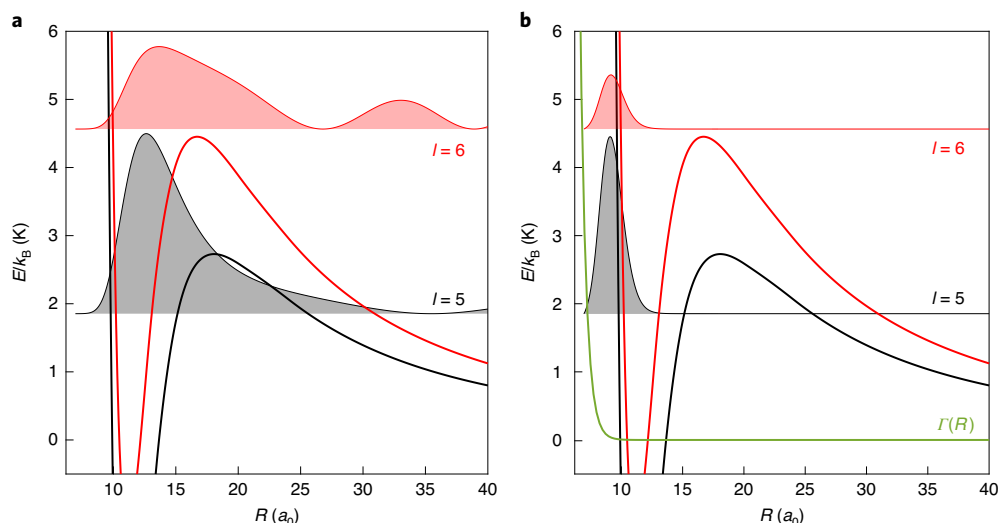


Fig. 4 | Partial wave analysis. a,b, The effective isotropic potential curves are presented as a function of the distance between He^+-D_2 in units of Bohr radii (a_0 ; $\sim 5.29 \times 10^{-11}$ m) together with the corresponding resonance wavefunctions squared (**a**) and the resonance wavefunctions squared multiplied by the Penning ionization rate $\Gamma(R)/\hbar$, shown in green (**b**). Black and red denote the partial wave channels $l=5$ and 6 , respectively. The shading illustrates the probability density for elastic scattering (**a**) and Penning ionization (**b**).

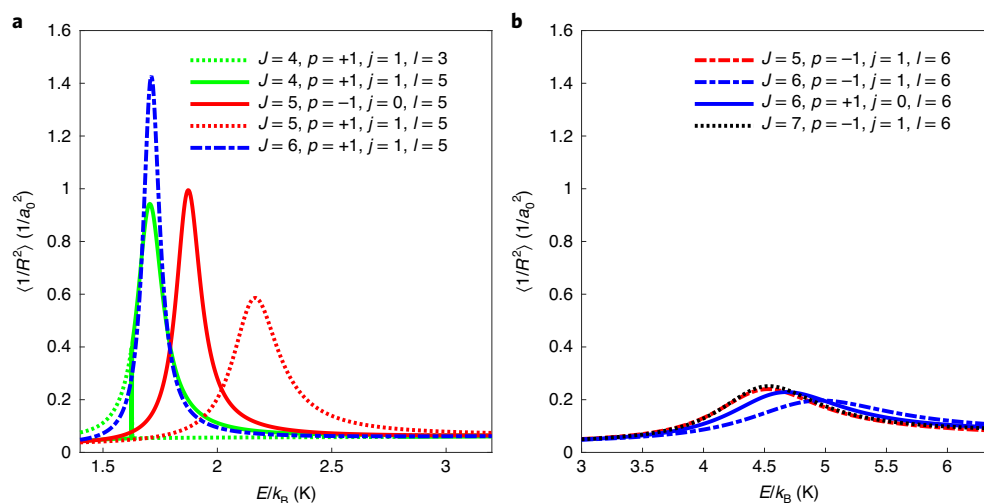


Fig. 5 | Characterization of resonances. Expectation value of $\langle 1/R^2 \rangle$ as a function of eigen state energy for *ortho*- ($j=0$) and *para*- D_2 ($j=1$) at 1.8 ± 0.1 K (**a**) and 4.4 ± 0.2 K (**b**). Here, p and l denote parity and partial wave, respectively.

however, in case of elastic collisions at the same energy this feature becomes a fully resolved resonance peak with the amplitude comparable with the low-energy resonance at 1.8 K. Furthermore, a new minor resonance peak appears at 7.8 K for elastic collisions. This indicates a different physical mechanism that is responsible for the formation of these two resonance states as compared with the major shape resonance observed in the reactive Penning ionization process.

To confirm the character of these resonances, we perform partial-wave analysis, where we calculate the resonance energies using the complex absorbing potential method³⁵ and the resonance wavefunctions using Numerov's algorithm. For simplicity, we consider only the isotropic part of the potential in this analysis. The probability density of the colliding particles, given by $|\psi|^2$, as a function of interparticle separation is indicated by the shaded regions in Fig. 4a for the two resonances at 1.8 K and 4.4 K, corresponding to

the $l=5$ (black) and $l=6$ (red) partial-wave channels, respectively. The energy of the $l=5$ resonance lies below the centrifugal barrier such that the amplitude is trapped behind the barrier—this is a shape resonance. By contrast, the energy of the $l=6$ resonance lies well above the peak of the centrifugal barrier (the same is true for the $l=7$ resonance); these are above the barrier orbiting resonances. A more rigorous analysis for identifying the contributions of different j and l to individual resonances is performed by calculating rotational constants (as illustrated in Fig. 5 and discussed in the Methods). The resonances at 1.8 ± 0.1 K, 4.4 ± 0.2 K and 7.8 ± 0.3 K are indeed formed with the primary contribution of a single partial wave, $l=5$, 6 and 7 , respectively, which dominates over the background. Due to different multiplicities in j , several J values contribute to a single resonance in the case of He^+ colliding with *para*- D_2 , where J is the total angular momentum. This is in contrast to He^+ colliding with *ortho*- D_2 , where $j=0$ and only a single J contributes

(note that the value of J ranges from $|j-l|$ to $|j+l|$); however, in the experiment, these structures are only visible as a single convoluted peak.

To explain why the $l=6$ and $l=7$ resonances were not observed in the Penning ionization reaction, we calculate the Penning ionization probability as a function of internuclear distance. This is obtained by scaling the probability density $|\psi|^2$ by the ionization rate $\Gamma(R)/\hbar$, which is approximated by a single exponential term and shown by the green curve in Fig. 4b, where $\Gamma(R)$ is taken from work by Yun et al.³⁶ The Penning ionization probability ($|\psi|^2\Gamma(R)$) of the $l=6$ resonance is clearly much smaller than that for $l=5$ due to the very strong weight that the ionization rate gives to the probability amplitude at the shortest distances. Although the $l=6$ above-barrier resonance shows some localization in its wavefunction (as shown in Fig. 4b), in agreement with the theoretical prediction for Penning ionization²⁷, it is not strong enough to considerably enhance Penning ionization, as is obvious from the blue curve in Fig. 3 (the same is true for $l=7$).

The combination of two state-of-the-art techniques—merged beams and high-resolution VMI—enables us to observe the resonances in the elastic collisions of He⁺ with D₂ at collision energies going down to a few kelvin, where two new resonance structures are revealed as compared with previously studied Penning ionization reaction. This suggests that a different resonance formation mechanism is in play. The dynamics of Penning ionization process can be naturally divided into the long-range part that is governed by centrifugal barriers and the short-range part that defines the reaction probability. This is a hallmark of a process that can be conveniently described by capture models³⁷. As such, we show that by comparing the elastic scattering process, which is sensitive to the whole internuclear interaction range, with the highly localized Penning ionization process, we can unambiguously differentiate between localized shape-type resonances and short-lived orbiting ones. We expect this approach to be general and applicable to other processes described by capture models.

Online content

Any methods, additional references, Nature Research reporting summaries, source data, extended data, supplementary information, acknowledgements, peer review information; details of author contributions and competing interests; and statements of data and code availability are available at <https://doi.org/10.1038/s41557-020-00578-x>.

Received: 3 February 2020; Accepted: 14 October 2020;

Published online: 30 November 2020

References

- Friedrich, H. *Scattering Theory* 2nd edn (Springer, 2016).
- Császár, A. G. et al. Rotational–vibrational resonance states. *Phys. Chem. Chem. Phys.* **22**, 15081–15104 (2020).
- Feshbach, H. Unified theory of nuclear reactions. *Ann. Phys.* **5**, 357–390 (1958).
- Fano, U. Effects of configuration interaction on intensities and phase shifts. *Phys. Rev.* **124**, 1866–1878 (1961).
- Chin, C., Grimm, R., Julienne, P. & Tiesinga, E. Feshbach resonances in ultracold gases. *Rev. Mod. Phys.* **82**, 1225–1286 (2010).
- Yang, H. et al. Observation of magnetically tunable Feshbach resonances in ultracold ²³Na⁴⁰K + ⁴⁰K collisions. *Science* **363**, 261–264 (2019).
- Clary, D. C. & Henshaw, J. P. Chemical reactions dominated by long-range intermolecular forces. *Faraday Discuss. Chem. Soc.* **84**, 333–349 (1987).
- Quémener, G. & Julienne, P. S. Ultracold molecules under control! *Chem. Rev.* **112**, 4949–5011 (2012).
- Schutte, A., Bassi, D., Tommasini, F. & Scoles, G. Orbiting resonances in the scattering of H atoms by mercury at thermal energies. *Phys. Rev. Lett.* **29**, 979–982 (1972).
- Toennies, J. P., Welz, W. & Wolf, G. Observation of orbiting resonances in the integral cross section of H–Xe. *J. Chem. Phys.* **61**, 2461–2462 (1974).
- Toennies, J. P., Welz, W. & Wolf, G. Observation of orbiting resonances in H₂–rare gas scattering. *J. Chem. Phys.* **64**, 5305–5307 (1976).
- Grover, J. R., Toennies, J. P., Welz, W. & Wolf, G. The observation of resonance maxima in H + CF₄ and H + SF₆ scattering. *Chem. Phys. Lett.* **48**, 24–28 (1977).
- Toennies, J. P., Welz, W. & Wolf, G. Molecular beam scattering studies of orbiting resonances and the determination of van der Waals potentials for H–Ne, Ar, Kr, and Xe and for H₂–Ar, Kr, and Xe. *J. Chem. Phys.* **71**, 614–642 (1979).
- Boesten, H. M. J. M., Tsai, C. C., Verhaar, B. J. & Heinzen, D. J. Observation of a shape resonance in cold-atom scattering by pulsed photoassociation. *Phys. Rev. Lett.* **77**, 5194–5197 (1996).
- Skodje, R. T. et al. Observation of a transition state resonance in the integral cross section of the F + HD reaction. *J. Chem. Phys.* **112**, 4536–4552 (2000).
- Qiu, M. et al. Observation of Feshbach resonances in the F + H₂ → HF + H reaction. *Science* **311**, 1440–1444 (2006).
- Manolopoulos, D. E. et al. The transition state of the F + H₂ reaction. *Science* **262**, 1852–1855 (1993).
- Kim, J. B. et al. Spectroscopic observation of resonances in the F + H₂ reaction. *Science* **349**, 510–513 (2015).
- Henson, A. B., Gersten, S., Shagam, Y., Narevicius, J. & Narevicius, E. Observation of resonances in Penning ionization reactions at sub-kelvin temperatures in merged beams. *Science* **338**, 234–239 (2012).
- Osterwalder, A. Merged neutral beams. *EPJ Tech. Instrum.* **2**, 10 (2015).
- Chefdévile, S., Kalugina, Y., van de Meerakker, S. Y. T., Lique, F. & Costes, M. Observation of partial wave resonances in low-energy O₂–H₂ inelastic collisions. *Science* **341**, 1094–1096 (2013).
- Vogels, S. N. et al. Imaging resonances in low-energy NO–He inelastic collisions. *Science* **350**, 787–790 (2015).
- Vogels, S. N. et al. Scattering resonances in bimolecular collisions between NO radicals and H₂ challenge the theoretical gold standard. *Nat. Chem.* **10**, 435–440 (2018).
- Bergeat, A. et al. Understanding the quantum nature of low-energy C(³P₁) + He inelastic collisions. *Nat. Chem.* **10**, 519–522 (2018).
- Beyer, M. & Merkt, F. Half-collision approach to cold chemistry: shape resonances, elastic scattering, and radiative association in the H⁺ + H and D⁺ + D collision systems. *Phys. Rev. X* **8**, 1–15 (2018).
- Ren, Z. et al. Probing the resonance potential in the F atom reaction with hydrogen deuteride with spectroscopic accuracy. *Proc. Natl Acad. Sci. USA* **105**, 12662–12666 (2008).
- Lavert-Ofir, E. et al. Observation of the isotope effect in sub-kelvin reactions. *Nat. Chem.* **6**, 332–335 (2014).
- Eppink, A. T. J. B. & Parker, D. H. Velocity map imaging of ions and electrons using electrostatic lenses: application in photoelectron and photofragment ion imaging of molecular oxygen. *Rev. Sci. Instrum.* **68**, 3477–3484 (1997).
- Ashfold, M. N. R. et al. Imaging the dynamics of gas phase reactions. *Phys. Chem. Chem. Phys.* **8**, 26–53 (2006).
- Even, U. The Even–Lavie valve as a source for high intensity supersonic beam. *EPJ Tech. Instrum.* **2**, 17 (2015).
- Klein, A. et al. Directly probing anisotropy in atom–molecule collisions through quantum scattering resonances. *Nat. Phys.* **13**, 3–5 (2017).
- Skodje, R. T. et al. Resonance-mediated chemical reaction: F + HD → HF + D. *Phys. Rev. Lett.* **85**, 1206–1209 (2000).
- Yang, T. et al. Extremely short-lived reaction resonances in Cl + HD ($v = 1$) → DCl + H due to chemical bond softening. *Science* **347**, 60–63 (2015).
- Wang, T. et al. Dynamical resonances in chemical reactions. *Chem. Soc. Rev.* **47**, 6744–6763 (2018).
- Moiseyev, N. *Non-Hermitian Quantum Mechanics* (Cambridge Univ. Press, 2011).
- Yun, R., Narevicius, E. & Averbukh, V. Penning ionization widths by Fano-algebraic diagrammatic construction method. *J. Chem. Phys.* **148**, 114101 (2018).
- Zhang, D. & Willitsch, S. in *Cold Chemistry: Molecular Scattering and Reactivity Near Absolute Zero* (eds Dulieu, O. & Osterwalder, A.) Ch. 10 (Royal Society of Chemistry, 2018).

Publisher's note Springer Nature remains neutral with regard to jurisdictional claims in published maps and institutional affiliations.

© The Author(s), under exclusive licence to Springer Nature Limited 2020

Methods

Experiment. Supersonic beams of He and D₂ are produced by adiabatically expanding neat gases at backing pressures of 35 bar via two pulsed (10 Hz) and cooled Even–Lavie valves³⁰. The D₂ beam is produced with a mean velocity ranging from 990–1,550 m s⁻¹ (speed ratio ≈ 30), generated by changing the temperature of the valve; the collision energy is tuned from 0.9 K to 50 K by changing the relative velocity between the two beams, keeping the He⁺ beam velocity constant. The measurement is carried out with normal D₂, which is two-thirds *ortho* and one-third *para*. The supersonic expansion used in the production of the beams creates D₂ in the lowest *j* states of its *ortho* and *para* components, which results in two-thirds of population in *j* = 0 and one-third in *j* = 1. The helium beam, produced with a mean velocity 906 m s⁻¹ (speed-ratio = 70), is excited to He⁺ by a dielectric barrier discharge³⁸ located at the valve orifice. Only the low-field-seeking Zeeman sublevel is confined to the two dimensions during the transit through the 20-cm-long magnetic guide. The valves are timed such that the He⁺ and D₂ beams arrive at the laser ionization volume (detection zone) located at the centre of the VMI set-up at the same time. Both the beams pass through 4-mm-diameter skimmers located 10 cm after the valve orifice. The D₂ beam then travels straight to the reaction chamber, whereas the He⁺ beam enters the magnetic guide, which has a 10° curve and is subsequently merged with the straight-propagating D₂ beam. The beams pass through a 3 mm aperture located at the entrance of the VMI set-up attached perpendicular to the beam propagation axis. The electrostatic lens in the VMI set-up consists of eight separate plates maintained at constant voltages throughout the measurement, followed by a ninth grounded plate. The first extractor plate, placed immediately above the repeller plate, has an aperture of 1 cm in diameter. The remaining seven plates have an aperture of 4 cm diameter. The voltages are distributed linearly from 2,000 V on the repeller plate to 1,160 V on the eighth plate to focus products on the MCP detector plane located after the ~1 m long grounded flight tube as shown in Fig. 1. A 260 nm laser (~10 μJ), obtained by doubling the output of an optical parametric oscillator laser, pumped by 355 nm pulsed (10 Hz) Nd:YAG source, is used to single-photon ionize the He⁺. The laser propagation axis is perpendicular to both the beam propagation axis and the VMI set-up. He⁺ ions thus formed are accelerated towards the phosphor screen located behind the VMI plates and MCP. The fluorescence generated from the electrons (formed from He⁺ hitting the MCP) as it impinges on the phosphor screen is then imaged on the camera. A real-time centroiding is performed to determine the *x*–*y* coordinate of each event on the MCP, thus correlating an electrical signal to the position and number of ions. The MCP is time-gated for detecting mass/charge of 4 AMU per *e* by applying a 50 ns high-voltage pulse to reduce the undesired ions from associative ionization and any other processes such as ionization of background gases by laser and He⁺. However, the collisions of He⁺ with D₂ also produce Penning ionization product D₂⁺, which has the same mass/charge as that of He⁺. Note that Penning ionization products can also be detected via VMI^{39,40}, nevertheless, their absence in our measurements is explained by several factors. The rate of Penning ionization between He⁺ and D₂ is at least 70-times slower (obtained from theoretical cross-sections) when compared with the partial rate coefficient (integrated over the backward hemisphere) in case of elastic collisions. D₂⁺ ions formed in the Penning ionization reaction are continuously extracted over period of 10 μs; He⁺ ions that are detected after photoionization arrive within 50 ns time window achieved by MCP gating. This provides another signal to background D₂⁺ ion ratio of 200 bringing the total signal to background ratio to 70 × 200 = 14,000. The detection of D₂⁺ is thus reduced by more than four orders of magnitude as compared to He⁺ and does not interfere with our measurements.

The VMI apparatus is calibrated by accumulating images at different relative velocities and then determining the shift in the centre of the images obtained, here the centre of the images corresponds to the centre-of-mass velocity of He⁺–D₂ pair. The velocity-per-camera pixel is determined to be 10.9 m s⁻¹ for He⁺. The experimental VMI images shown in Fig. 2 are obtained by binning the *x*–*y* coordinates of each MCP event onto a 2D array with a mesh spacing equal to 0.5 camera pixel. These images are normalized by dividing each element of the 2D array by the total intensity in respective backward hemispheres and subsequently multiplying by the partial rate coefficient for that energy. All images are represented on the same colour scale where the maximum is set to the highest intensity for the image corresponding to 1.8 K. The angular distribution for the images is evaluated by integrating the intensity in an annulus whose edges are determined by the width of the intense ring visible in all VMI images. Here, the angular grid spacing is taken to be 3.6° inside the annulus.

We characterize the He⁺ beam by counting the number of He⁺ atoms present in the same ionization region in the absence of the D₂ beam. This is achieved by defocusing the He⁺ signal on the VMI camera after single-photon ionization using a 260 nm laser. As more than ten ions are present in each ionization event, we defocus the He⁺ ions by changing the voltage on the first extractor plate of our VMI apparatus, increasing the spot size to a dimension that allows convenient separation between individual ions. A separate MCP placed on-axis with the direction of propagation of the beams is also used to characterize the He⁺ beam. The D₂ beam is characterized by a time-of-flight mass spectrometer⁴¹ positioned perpendicular to the beam propagation direction, using an ionization filament to form D₂⁺. The time-of-flight mass spectrometer is used in multipulsed mode with 10 μs intervals to obtain the longitudinal profile of the beam. At any given collision

energy, the partial rate coefficient is obtained by scaling the number of He⁺ atoms scattered in the backward hemisphere of the VMI image and collected for 21,000 laser shots by the product of number of He⁺ in the reactant beam and D₂ beam intensity, averaged over 1,500 laser shots and 100 shots respectively.

Theory. To obtain cross-sections and rate coefficients, close-coupling quantum scattering calculations have been performed for collisions with *ortho*- (*j* = 0) and *para*-D₂ (*j* = 1), using the theoretical framework established in work by Klein et al.³¹ The angular basis functions are constructed as products of the rotational state of the D₂ molecule and the partial wave describing the orbital motion of the whole complex and are symmetry-adapted to the values of *J* and the spectroscopic parity. The basis set is restricted to even (odd) rotational states of the dimer for collisions with *ortho*-D₂ (*para*-D₂). Differential elastic and inelastic scattering cross-sections for energies up to 50 K are obtained using a basis set including all of the relevant functions with *J* ≤ 30. This converges our results to an accuracy of below 1% even for the highest scattering energies considered. The scattering wavefunctions are obtained by propagating from 7 *a*₀ to 200 *a*₀ by means of a renormalized Numerov propagator. Short-range and asymptotic boundary conditions are imposed afterwards, as described in work by Janssen et al.⁴² The final cross-section used in the simulations (described below) are the weighted average of the *ortho*- and *para*-D₂ cross-sections.

Scattering resonances are identified by diagonalization of the nuclear Hamiltonian describing collisions between He⁺ and molecular deuterium for fixed *J* and spectroscopic parity. The corresponding potential energy surface is adopted from Klein et al.³¹, where it had been used to obtain resonance positions and the overall behaviour of rate coefficient for the electronically identical He⁺–H₂ system, yielding excellent agreement between theoretical results and measured data. Here, for the He⁺–D₂ case, a mapped grid using 6,144 grid points and ranging from 2 *a*₀ to 20,000 *a*₀ is employed for the diagonalization, in conjunction with a Fourier-basis representation of the kinetic energy operator and a transmission-free complex absorbing potential at the outer boundary⁴³. Resonances are identified as local maxima of the expectation value of the rotational constant ($\langle 1/R^2 \rangle$) as a function of energy⁴⁴, which is illustrated in Fig. 5 for the resonances at 1.8 ± 0.1 K and 4.4 ± 0.2 K. These clearly have a predominantly *l* = 5 and *l* = 6 character, respectively. As only *J* is a good quantum number, the scattering states may have contributions from several *l*. We take a scattering state to be of primary *l*-character if 50% or more of its population resides in that *l*-channel. For all *J* quantum numbers contributing to the resonance around 4.4 K, we observe *l* = 6 character for their full energetic width. The same behaviour can be observed for the resonance with *l* = 5 character around 1.8 K with a minor exception: for *J* = 4 and positive parity the character of the resonance flips from *l* = 3 (dashed green curve in Fig. 5) to *l* = 5 (solid green curve in Fig. 5) at the resonance's left tail at about 1.62 K. This slight anomaly can also be observed when looking at the diabatic population in the *l* = 5 state, which is only slightly larger than 60% at the resonance peak. Conversely, for all other scattering states with large ($\langle 1/R^2 \rangle$) that we show in Fig. 5a,b, the diabatic population in the *l* = 5 and *l* = 6 states, respectively, is ≥ 95%. This indicates that the anisotropy-induced coupling between the diabatic *l* surfaces is larger for the *J* = 4 He⁺–*para*-D₂ resonance than in all other cases we have investigated.

Simulation details. The detection method employed in our experiment measures the partial relative rate coefficient and the angular distribution of the elastically scattered products. To convert the theoretical cross-sections into experimental observables, we have developed a computer program to simulate the He⁺–D₂ elastic scattering, taking into consideration the full kinematics of the experiment.

In the simulation, the two supersonic beams are assumed to have a Gaussian profile in velocity and temporal space. The mean velocities and the velocity spreads of the beams are known from the beam characterization described above; however, the temporal spread of the beams are not known, and thus we have optimized this parameter to achieve best fit to the experiment. In the experiment, the time difference between the valves is adjusted such that the beams exactly overlap only at the centre of the VMI set-up, however, the interaction region starts at the exit of the magnetic guide (where the tail ends of the Gaussian beams start overlapping) and continues all of the way until the detection zone. Accordingly, in the simulation, the initial interaction time (*t*₀) is defined as the time when the He⁺ beam exits the magnetic guide and the final interaction time (*t*_{laser}), as the time when the laser is fired. All collisions taking place between time *t*₀ and *t*_{laser} are considered. For any given time *t* (*t*₀ ≤ *t* ≤ *t*_{laser}), the number of scattered He⁺ particles formed at any position of the interaction region is assumed to be proportional to the overlap of the reactant beams and the theoretical rate coefficient (obtained by multiplying the theoretical integrated cross-section with the relative velocity). The elastically scattered He⁺ particles are distributed over a Newton sphere according to the theoretically obtained DCS. The radius of this sphere is calculated from conservation of energy and momentum. The scattered products at different collision energies expand with different laboratory-frame velocities, and the simulation corrects for any velocity dependent detection bias in the experiment. To determine the final position of the particles, the scattered He⁺ particles are propagated with their post collision lab-frame velocities from time *t* to *t*_{laser}. All of the particles that lie outside the 3 mm aperture located at the entrance of the VMI are discarded.

For evaluation of the theoretical partial relative rate coefficient, only the particles distributed over the backward hemisphere that arrive at the detection zone are counted and then normalized by the intensity of the reactant beams. Note that the laser ionization volume is estimated from the lens used to focus the laser beam. This process is repeated for every collision energy to obtain the black curve in Fig. 3. However, for the simulation of VMI images, all of the particles that arrive at the detection zone are considered. The images obtained at a given collision energy are simulated by projecting 3D spheres of elastically scattered He⁺ within the detection zone onto a 2D array with a mesh spacing of 1 m s⁻¹. The normalization and the evaluation of angular distributions for the simulated images shown in Fig. 2 is performed following the same procedure as for the experimental images.

Data availability

The data that support the findings of this study are available from the corresponding authors on reasonable request. Source Data for Fig. 3 is provided with the paper.

References

- Luria, K., Lavie, N. & Even, U. Dielectric barrier discharge source for supersonic beams. *Rev. Sci. Instrum.* **80**, 104102–104104 (2009).
- Blech, A. et al. Phase protection of Fano-Feshbach resonances. *Nat. Commun.* **11**, 999 (2020).
- Margulis, B., Narevicius, J. & Narevicius, E. Direct observation of a Feshbach resonance by coincidence detection of ions and electrons. *Nat. Commun.* **11**, 1–6 (2020).
- Wiley, W. C. & McLaren, I. H. Time-of-flight mass spectrometer with improved resolution. *Rev. Sci. Instrum.* **26**, 1150–1157 (1955).
- Janssen, L. M. C., van der Avoird, A. & Groenenboom, G. C. Quantum reactive scattering of ultracold NH(X³Σ⁻) radicals in a magnetic trap. *Phys. Rev. Lett.* **110**, 1–5 (2013).
- Manolopoulos, D. E. Derivation and reflection properties of a transmission-free absorbing potential. *J. Chem. Phys.* **117**, 9552–9559 (2002).
- Londoño, B. E., Mahecha, J. E., Luc-Koenig, E. & Crubellier, A. Shape resonances in ground-state diatomic molecules: general trends and the example of RbCs. *Phys. Rev. A* **82**, 012510 (2010).

Acknowledgements

We acknowledge financial support from the European Research Council and the Israel Science Foundation. Additional financial support from the German–Israeli Foundation (grant no. 1254) is gratefully acknowledged. C.P.K. is grateful for a Rosi and Max Varon Visiting Professorship. Correspondence and requests for materials should be addressed to E.N. and C.P.K.

Author contributions

P.P. and N.D. carried out the experiments. D.M.R. performed the calculations with help from A.v.d.A. C.P.K. and E.N. conceived and supervised the work. All authors discussed the results and wrote the manuscript.

Competing interests

The authors declare no competing interests.

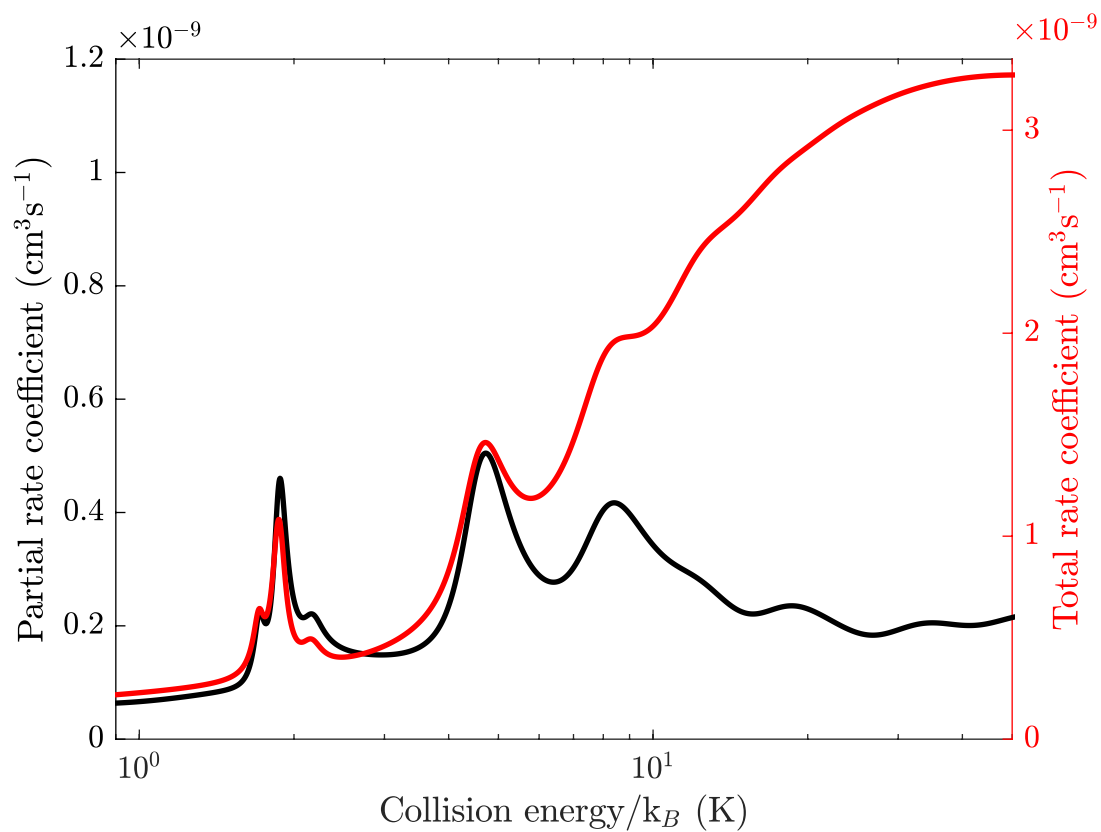
Additional information

Extended data is available for this paper at <https://doi.org/10.1038/s41557-020-00578-x>.

Supplementary information is available for this paper at <https://doi.org/10.1038/s41557-020-00578-x>.

Correspondence and requests for materials should be addressed to C.P.K. or E.N.

Reprints and permissions information is available at www.nature.com/reprints.



Extended Data Fig. 1 | Partial and total rate coefficients for elastic scattering of He^+ with normal D_2 . The black curve denotes the partial elastic scattering rate coefficient integrated only over the backward hemisphere. The red curve denotes the total elastic scattering rate coefficient (integrated over all scattering angles). Note the different y-scales for the partial and total rate coefficients.